



CrossMark  
click for updates

Cite this: *Energy Environ. Sci.*, 2015, 8, 195

Received 24th September 2014  
Accepted 27th October 2014

DOI: 10.1039/c4ee03045a

www.rsc.org/ees

## NaTiO<sub>2</sub>: a layered anode material for sodium-ion batteries†

Di Wu,<sup>‡a</sup> Xin Li,<sup>‡b</sup> Bo Xu,<sup>b</sup> Nancy Twu,<sup>b</sup> Lei Liu<sup>b</sup> and Gerbrand Ceder<sup>\*b</sup>

We report on layered NaTiO<sub>2</sub> as a potential anode material for Na-ion batteries. The material is prepared from only earth-abundant elements, delivers 152 mA h g<sup>−1</sup> of reversible capacity at C/10 rate, shows excellent cyclability with capacity retention over 98% after 60 cycles, and high rate capability. Furthermore, *in situ* X-ray diffraction analysis reveals a reversible O3–O'3 phase transition, including an unusual lattice parameter variation coupled to complicated Na vacancy orderings in a series of 2nd order phase transitions.

Sodium-ion batteries have attracted increasing attention for large-scale energy storage applications because of the natural abundance and low cost of sodium resources.<sup>1–3</sup> Na has a larger ionic radius (0.97 Å) and higher redox potential (−2.71 V vs. SHE) than Li, and the interactions between Na ions and the host crystal structures can vary greatly from those of their Li analogues,<sup>4</sup> which is why Na-intercalation in compounds is often very different from the behavior of the Li-analogues.<sup>1–4</sup> The most commonly applied anode material in Li-ion batteries is graphite, for which Na-ion intercalation is thermodynamically not favourable.<sup>5</sup> Currently, reports on applicable anode materials for Na-ion batteries are limited in the literature,<sup>1–3</sup> as summarized in Fig. 1. Hard carbon exhibits a reversible capacity of 240 mA h g<sup>−1</sup> with stable cycle performance in a NaClO<sub>4</sub>/EC:DEC electrolyte.<sup>6</sup> However, its density is very low, and most of the usable capacity is located near the sodium plating voltage, leading to potential safety concerns. Alloys such as Sn and Sb have been shown to exhibit very high storage capacities (~600 mA h g<sup>−1</sup>); however, undesired large volume change during sodium insertion and extraction makes it challenging to attain satisfactory cyclability without the use of special binders

### Broader context

Lithium-ion batteries are currently the energy storage technology of choice in portable electronic devices and electric vehicles. In recent years, sodium-ion batteries have been actively restudied as a promising alternative because of the abundance of sodium resources and the high capacity cathodes available. But as graphitic carbon can not be used as anode material, as it is in lithium batteries, the design of the novel Na-ion anode materials with high capacity and cycling-stability is critical for the advancement of Na-ion batteries. In this paper, we successfully synthesized and tested the layered NaTiO<sub>2</sub> compound with high reversible capacity and excellent cycling performance. The details of structural evolution and fundamental intercalation mechanism upon charging and discharging are revealed by *in situ* X-ray diffraction. Our findings will facilitate the development of novel electrode materials for sodium-ion batteries.

and electrolyte additives, and to achieve high enough effective energy density.<sup>7–10</sup> In addition, alloy anodes suffer from large capacity losses (150–500 mA h g<sup>−1</sup>) during initial sodiation. Oxides have also been explored as potential electrode candidates for Na-ion batteries.<sup>1–3,11</sup> Na<sub>2</sub>Ti<sub>3</sub>O<sub>7</sub> delivers an initial capacity of more than 200 mA h g<sup>−1</sup>; however, its cycling performance is not satisfactory.<sup>12,13</sup> Li<sub>4</sub>Ti<sub>5</sub>O<sub>12</sub> can deliver a reversible capacity of 155 mA h g<sup>−1</sup> in a displacement reaction with Na, and shows good cyclability using carboxymethyl-cellulose as the binder.<sup>14</sup> A new anode material, P2-Na<sub>0.66</sub>–[Li<sub>0.22</sub>Ti<sub>0.78</sub>]O<sub>2</sub>, exhibits excellent cyclability partly due to its negligible volume change (0.77%) during sodium insertion and extraction; however, the usable capacity is limited to 100 mA h g<sup>−1</sup>, corresponding to 1/3 Na per formula unit.<sup>15</sup>

Research on layered NaMO<sub>2</sub>-type oxides (M = 3d transition metal, such as Ti, V, Cr, Mn, Fe, Co, Ni) as intercalation electrode materials began in the 1980s but has recently received renewed interest.<sup>16–29</sup> Using advances in electrolytes, a re-investigation of NaMnO<sub>2</sub> and NaNiO<sub>2</sub> demonstrated that these compounds can reversibly exchange approximately 0.8 Na and 0.5 Na,<sup>22,23</sup> respectively, noticeably larger than the results previously reported in the 1980s.<sup>18,20</sup> In the 1980s, Mazzaz *et al.*

<sup>a</sup>Department of Mechanical Engineering, Massachusetts Institute of Technology, Cambridge, MA 01239, USA

<sup>b</sup>Department of Materials Science and Engineering, Massachusetts Institute of Technology, Cambridge, MA 01239, USA. E-mail: gceder@mit.edu

† Electronic supplementary information (ESI) available. See DOI: 10.1039/c4ee03045a

‡ These authors contributed equally.

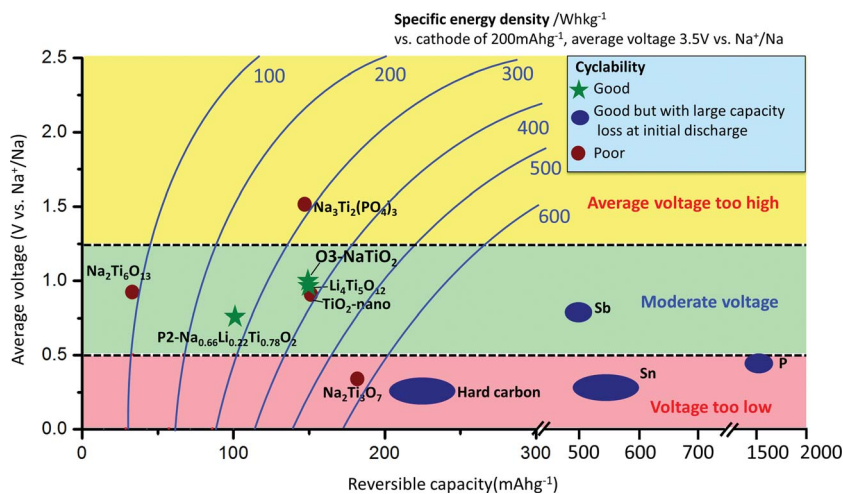


Fig. 1 Average voltage versus reversible capacity for various reported anode materials for Na-ion batteries. Lines of constant specific energy density are also shown, assuming a cathode of 200 mA h g<sup>-1</sup> at 3.5 V average voltage. The specific energy density is calculated from full cells with a balanced weight of anode and cathode. The cycling performance is based on literature reports.

examined the electrochemical performance of NaTiO<sub>2</sub> (ref. 19) as a potential anode intercalation material. However, limited cyclable capacity corresponding to  $\approx 0.3$  Na was reported. A recent DFT calculation hinted at an unusually high barrier of 0.75 eV for Na migration in NaTiO<sub>2</sub>,<sup>15</sup> which would prevent intercalation at any reasonable rate.

In this paper the performance of NaTiO<sub>2</sub> is re-investigated. In contrast to the previous work, an electrochemical reversible capacity of 152 mA h g<sup>-1</sup> is achieved, corresponding to approximately 0.5 Na exchange, with excellent cyclability and good rate capability. Our DFT simulation reveals very low Na diffusion barriers, consistent with the excellent electrochemical performance. *In situ* X-ray diffraction (XRD) reveals a complicated process of superstructure evolution coupled to an unusual lattice parameter variation during Na de-intercalation. Understanding this process may further help in the design of better Na-intercalation electrode materials.

## Results

NaTiO<sub>2</sub> was synthesized *via* a solid-state reaction using Na metal to reduce anatase TiO<sub>2</sub>.<sup>19</sup> The XRD spectrum and SEM image of the as-prepared NaTiO<sub>2</sub> powder are presented in Fig. 2, which shows a pure O3-type NaTiO<sub>2</sub> phase of space group *R*-3*m* with particle size of approximately 1 to 2  $\mu$ m. The "O3" nomenclature is after Delmas<sup>30</sup> and indicates that the Na ions are octahedrally coordinated by oxygen and have a repetition period of three transition metal stacking along the *c*-axis.<sup>30</sup> Rietveld refinement gives hexagonal lattice parameters of  $a = b = 3.037(1)$  Å and  $c = 16.260(2)$  Å, which is consistent with previous reports.<sup>19,31</sup> Another equivalent definition of the unit cell, which is often used to describe the phase with monoclinic distortion,<sup>16,29</sup> is illustrated in Fig. 2(a) together with the hexagonal definition. The corresponding lattice parameters of pristine NaTiO<sub>2</sub> to the two equivalent definitions are listed in the inset table in Fig. 2(c). Using an approach developed

recently in the NaCoO<sub>2</sub> system,<sup>32</sup> we find the Na content of the compound by comparing the *c* lattice parameter with the ones measured by *in situ* XRD at different Na intercalation levels

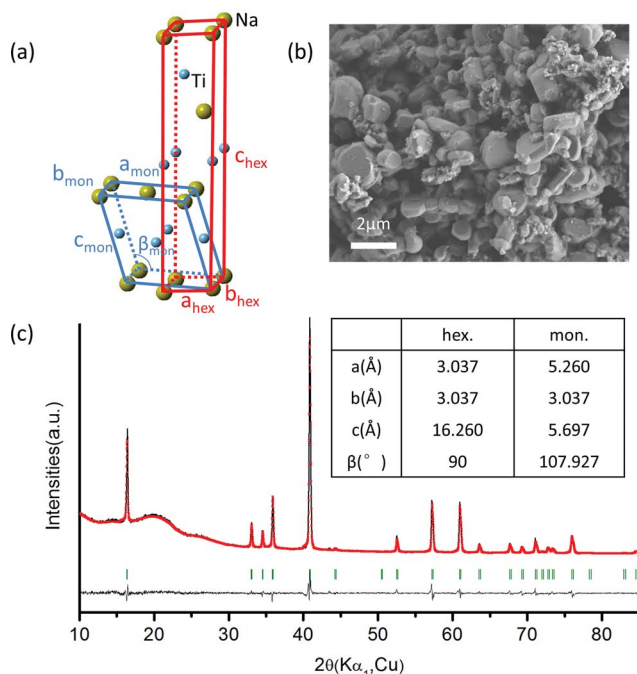


Fig. 2 (a) Schematic illustration of O3-type and O'3-type structures. The yellow and blue spheres represent Na and Ti, respectively. (b) SEM image of as-prepared NaTiO<sub>2</sub>, which shows an average particle size of 1 to 2  $\mu$ m. (c) X-ray diffraction pattern and Rietveld refinement of the as-prepared O3 NaTiO<sub>2</sub>. The Bragg peak positions are indicated by the short vertical lines. The black (red) line represents the experimental (calculated) data. The background and three broad peaks between 10°–30° originate from the Kapton film used to seal the sample. The refinement results are performed in the *R*-3*m* space group and yield  $R_{wp} = 11.06\%$  and goodness of fit = 1.28. In the inset, lattice parameters in a monoclinic cell are given for comparison with that of the hexagonal cell.

(Fig. S1†). This analysis yields a composition close to  $\text{Na}_{0.99}\text{TiO}_2$ , which is consistent with previous reports.<sup>31,33</sup>

A battery was assembled as  $\text{NaTiO}_2 | 1 \text{ M NaPF}_6 \text{ in EC : DEC} = 1 : 1 | \text{Na}$ . The electrolyte was dehydrated using molecular sieves, with details provided in the Methods. The electrochemical performance of  $\text{NaTiO}_2$  is shown in Fig. 3.  $\text{NaTiO}_2$  delivers  $152 \text{ mA h g}^{-1}$  of reversible capacity in the voltage range of 0.6–1.6 V, corresponding to approximately 52% of the theoretical capacity based on a single-electron redox process of the  $\text{Ti}^{3+}/\text{Ti}^{4+}$  couple (theoretical capacity of  $293.3 \text{ mA h g}^{-1}$  calculated based on the partial desodiated compound  $\text{Na}_{0.5}\text{TiO}_2$ ). The capacity is among the highest of anode intercalation compounds, as evidenced by Fig. 1. The strong similarity between the discharge and charge curves and the low 0.02 V hysteresis at the voltage plateau shown in Fig. 3(a) indicates that the intercalation process is reversible with only small polarization.

When raising the lower voltage cutoff, a specific capacity of approximately  $109 \text{ mA h g}^{-1}$  in the voltage range of 0.8–1.6 V (0.37 Na) is achieved as shown in Fig. 3(d), which is slightly larger than the previously reported value.<sup>19</sup> It is noteworthy that in the low-voltage range from 0.6 V to 0.8 V,  $\text{NaTiO}_2$  delivers an additional capacity of approximately  $45 \text{ mA h g}^{-1}$  (0.15 Na). We notice that the open-circuit-voltages of as-prepared batteries fall into this voltage window, which might be due to different levels of Na self-deintercalation from battery to battery. However, the capacity in the low-voltage range derives from a reversible intercalation reaction, as confirmed by the continuous decrease

of the slab distance of  $\text{Na}_x\text{TiO}_2$  upon Na intercalation down to 0.6 V (Fig. S1†) and a reverse process upon Na de-intercalation identified by *in situ* XRD. Identification of this reversible electrochemical reaction in the low voltage range not only results in capacity that is 50% higher than previous reports,<sup>19</sup> but more importantly, it gives the correct relation between Na composition and electrochemical voltage for further structure and superstructure analysis.

If the lower cutoff voltage is further decreased to 0.55 V, cycle life decreases as demonstrated in Fig. S2,† likely due to the electrolyte decomposition.<sup>6</sup> If charged above 1.6 V, an irreversible structure modification is observed in our *in situ* XRD results (Fig. S3†), in accordance with a previous *ex situ* XRD study.<sup>19</sup> We thus restricted the voltage window to 0.6–1.6 V. Fig. 3(b) shows that in the 0.6–1.6 V voltage range  $\text{NaTiO}_2$  retains 98% of its initial capacity after 60 cycles at a current rate of C/10. The coulombic efficiency is approximately 82% in the initial cycle and 99.5% in the later cycles, which is comparable to the behavior of some of the best anode materials.<sup>14,15</sup>

The rate capability of  $\text{NaTiO}_2$  is shown in Fig. 3(c). At C/5 rate, a charge capacity of  $152 \text{ mA h g}^{-1}$  (99% of C/10 rate) is achieved with excellent cyclability. Even at 1 C rate, the compound still delivers a large charge capacity of  $133.6 \text{ mA h g}^{-1}$  (87.9% of C/10 rate) with a small polarization of the voltage curve. Note that special treatment of the electrode material such as carbon coating or nanosizing may further improve the electrochemical performance from the micrometer-sized  $\text{NaTiO}_2$

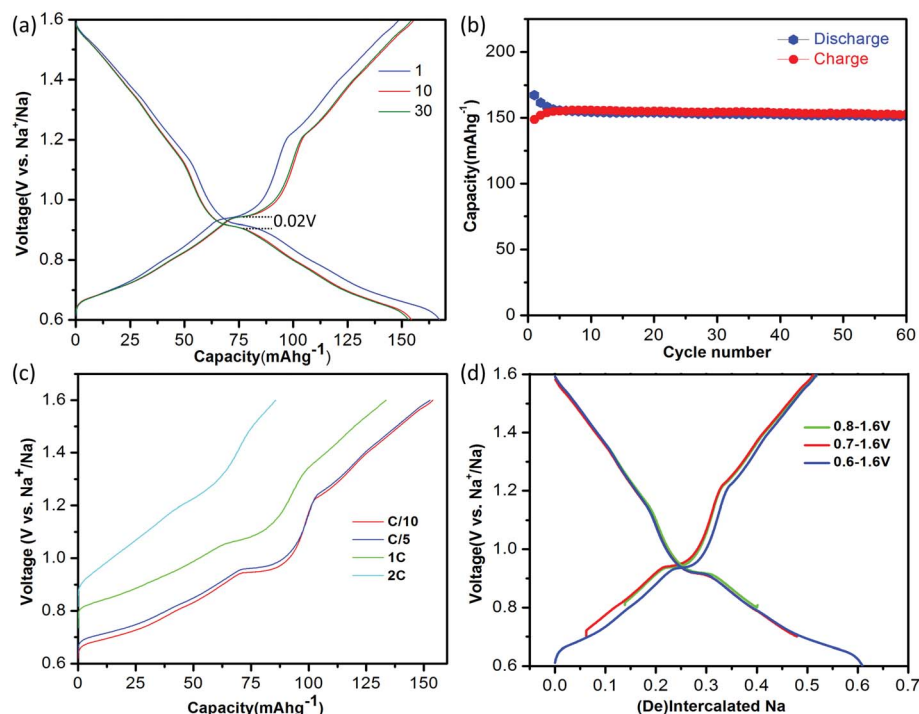


**Fig. 3** Electrochemical performance of  $\text{NaTiO}_2$ . (a) The 1st, 10th and 30th galvanostatic charge/discharge curves at a current rate of C/10 in the voltage range of 0.6–1.6 V versus  $\text{Na}^+/\text{Na}$ . The voltage curve of the battery pre-discharged to 0.6 V is not shown for simplicity (see ESI Fig. S1(b)†). (b) Cyclability. The charge/discharge capacity versus cycle number at a current rate of C/10. (c). Rate capability. The battery was discharged to 0.6 V at a current rate of C/20 and then charged to 1.6 V at different rates from C/10 to 2 C. (d) Comparison of the amount of cycled Na in voltage windows with lower cut-off voltages from 0.6–0.8 V.



particles.<sup>34</sup> The average voltage of sodium insertion into NaTiO<sub>2</sub> is approximately 1 V, which is higher than previous report for P2-Na<sub>0.66</sub>[Li<sub>0.22</sub>Ti<sub>0.78</sub>]O<sub>2</sub>.<sup>15</sup> However, as observed in Fig. 1 and ESI Table 1,<sup>†</sup> full cells assembled with NaTiO<sub>2</sub> anode and appropriate cathodes could still achieve a considerably higher energy density due to the relatively larger capacity of NaTiO<sub>2</sub>.

The structural evolution in Na<sub>x</sub>TiO<sub>2</sub> upon electrochemical de-intercalation as measured by *in situ* XRD is illustrated in Fig. 4. In the 0.6–0.94 V range, the positions of the diffraction peaks shift continuously, suggesting a typical single-phase domain. XRD refinement reveals that the O3 phase with hexagonal *R*-3*m* symmetry is maintained in the corresponding composition range of  $1 > x > 0.76$  in Na<sub>x</sub>TiO<sub>2</sub>. Upon further sodium deintercalation at the 0.94 V voltage plateau, the (003)<sub>hex</sub> diffraction peak broadens together with the appearance of a new adjacent peak at lower angle, and the split of (01-4)<sub>hex</sub> diffraction peak into two peaks, suggesting a two-phase domain, which is observed to be reversible in the discharge process.

The diffraction peaks of the new phase can be indexed by the O'3-type layered structure with monoclinic space group

*C2/m*.<sup>19,30</sup> Rather than the 108°  $\beta$  angle in the O3 phase (converted to the monoclinic definition as illustrated in Fig. 2(a)), the  $\beta$  angle of the O'3 phase is approximately 106°, displaying a monoclinic distortion, which features the splitting of the (01-4)<sub>hex</sub> reflection into (111)<sub>mon</sub> and (20-2)<sub>mon</sub> reflections as shown in Fig. 4. When charged close to 1.54 V or Na<sub>0.5</sub>TiO<sub>2</sub>, the distance between the (111)<sub>mon</sub> and (20-2)<sub>mon</sub> peaks decreases and they tend to merge, indicating a transform back toward the hexagonal structure.<sup>19,33</sup> Cyclic voltammetry results at various sweep rates and the first differential capacity curve (dQ/dV) further confirm a typical intercalation reaction mechanism, as shown in Fig. S4.<sup>†</sup>

The corresponding evolution of lattice parameters during sodium deintercalation is illustrated in Fig. 5. In the O3 phase region, the shift of the (003) diffraction peak to lower  $2\theta$  angles demonstrates that the interslab distance  $d_{003}$ , which is 1/3 of the  $c_{\text{hex}}$  parameter, increases due to the loss of cohesiveness when sodium ions are extracted from the interslab space,<sup>30</sup> as illustrated in Fig. 5(a). In addition, due to the oxidation of titanium, the  $a_{\text{hex}}$  parameter, which measures the average Ti–Ti ion distances decreases.

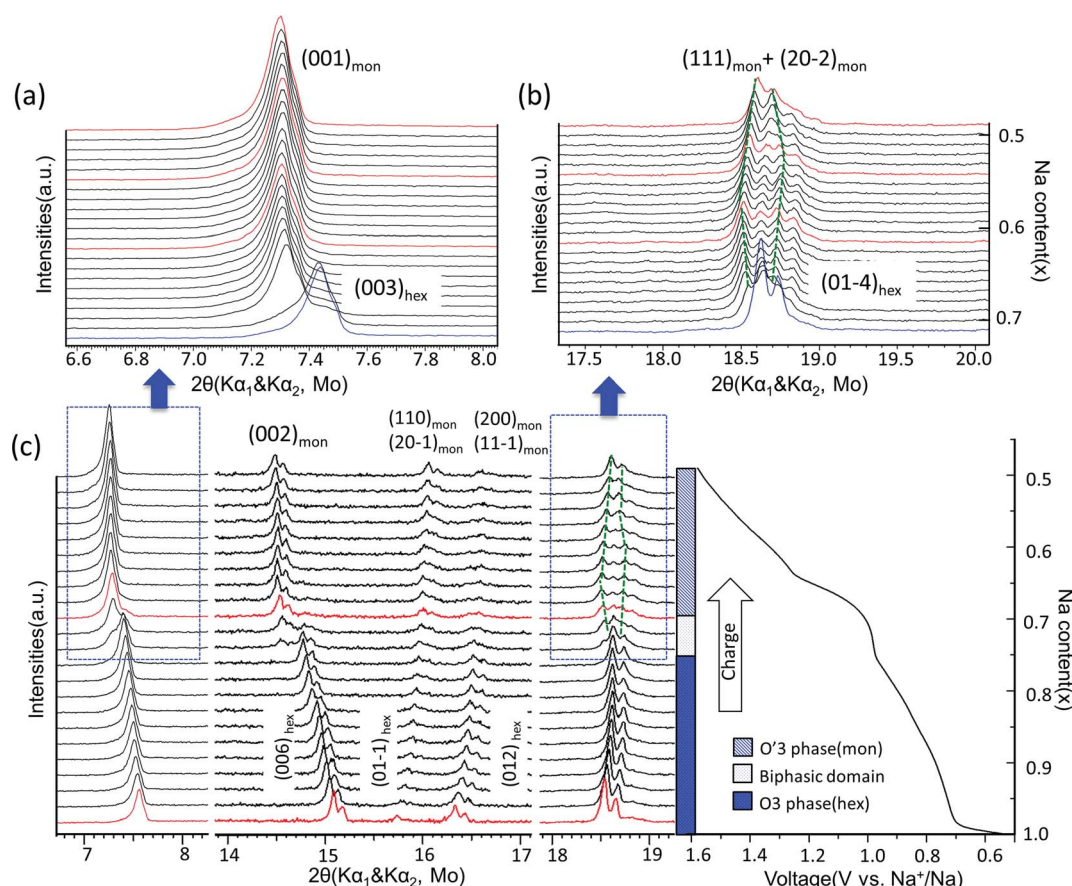


Fig. 4 Structural evolution during electrochemical desodiation of O3-NaTiO<sub>2</sub>. (a) and (b) *In situ* X-ray diffraction patterns recorded during the PITT experiments centered around the (003)<sub>hex</sub>, (001)<sub>mon</sub> reflections and (01-4)<sub>hex</sub>, (111)<sub>mon</sub> + (20-2)<sub>mon</sub> reflections, respectively. Note that X-ray source is Mo with K $\alpha_1$  and K $\alpha_2$ . The green dash lines illustrate the evolution of K $\alpha_1$  reflections in O'3 phase region. The red XRD spectra are further explained in Fig. 6. (c) *In situ* XRD patterns during the first galvanostatic charge at a current rate of C/20 in the voltage range between 0.5 V and 1.6 V. The regions corresponding to (a) and (b) are marked by the dashed boxes. Note that in the entire  $2\theta$  range, preferred orientation for (00l) reflections exists because the electrode films were prepared using a dry method that involved multiple pressing and rolling processes.

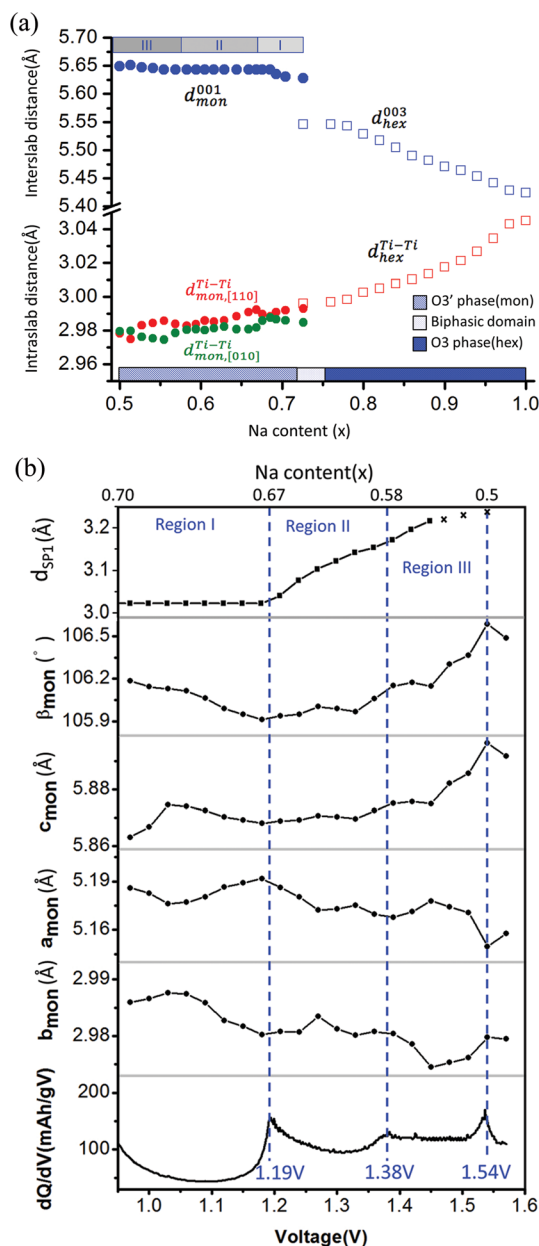


Fig. 5 (a) Interslab and intraslab distances in the  $Na_xTiO_2$  phases. The interplanar distances are calculated using the following equations:  $d_{hex}^{003} = c_{hex}/3$ ,  $d_{hex}^{Ti-Ti} = a_{hex}$ ,  $d_{mon}^{001} = c_{mon} \sin \beta_{mon}$ ,  $d_{mon, [110]}^{Ti-Ti} = \frac{1}{2} \sqrt{a_{mon}^2 + b_{mon}^2}$ ,  $d_{mon, [010]}^{Ti-Ti} = b_{mon}$ . (b) Correlation between the evolution of lattice parameters of the O'3 phase and differential capacity curve in the voltage range of 0.95 V–1.57 V. The  $a_{mon}$ ,  $b_{mon}$ ,  $c_{mon}$  and  $\beta_{mon}$  cell parameters were determined from *in situ* X-ray diffraction patterns collected during PITT charge with a 4 h scan per spectrum and a 0.03 V voltage step. The cell parameters were calculated using a conventional monoclinic unit cell with  $C2/m$  symmetry. Regions I, II, and III are divided by the three inflection points on the 1st differential curve of capacity over voltage.  $d_{SP1}$  represents the interplanar distance of the strongest superstructure peak labeled in Fig. 6.

To improve the precision of the calculated lattice parameters and observe clearly the superstructure evolution in the O'3 region, X-ray spectra were collected while the *in situ* battery was

held potentiostatically at each voltage step between 0.97 V and 1.57 V, with a 0.03 V step size. In the O'3 single-phase region, the  $(001)_{mon}$  and  $(002)_{mon}$  peaks remain in the same  $2\theta$  position (Fig. 4(a)), corresponding to a constant interslab distance upon deintercalation shown in Fig. 5(a). In addition to the phenomena of constant slab distance, the in plane Ti–Ti ion distance continuously modulates upon desodiation within a narrow range of 0.02 Å in the O'3 phase, as also illustrated in Fig. 5(a). In Fig. 5(b), the variations of lattice parameters of the O'3 phase at different PITT voltages were compared with the 1st derivative of the galvanostatic charge capacity over voltage, which reveals three inflection points at 1.19 V, 1.38 V and 1.54 V dividing the O'3 phase into three regions. The 2nd derivative of the capacity over voltage is discontinuous at these three voltage points, indicating 2nd order phase transitions.<sup>35</sup> Compared with the typical trend of lattice parameter evolution observed in the O3 single phase region, it is quite unusual that in the O'3 phase region, the inter- and intra-slab distances vary in such a narrow range upon Na de-intercalation, which may indicate the existence of some unusual Na orderings.

Superstructure evolution with varying sodium content is in fact observed using *in situ* XRD as shown in Fig. 6, which reveals the presence of additional weak Bragg peaks that are characteristic of superstructures in the  $12^\circ$ – $14^\circ$  and  $17^\circ$ – $18^\circ$   $2\theta$  range. The strongest superstructure peak appears at approximately  $13.5^\circ$  (SP1) and remains at the same angle in region I until the battery is charged up to the inflection point at 1.19 V (corresponding to  $\sim Na_{0.67}TiO_2$ ). Beyond the inflection point, this peak starts to shift to lower  $2\theta$  angles during the desodiation process in region II. A similar behavior is simultaneously observed for the superstructure peaks at approximately  $17.9^\circ$  (SP2). These superstructure peaks undergo a very significant shift, their rate of change in diffraction angle being an order of magnitude larger than the major  $hkl$  peak shift of the O'3 phase, as shown for SP1 in region II of Fig. 5(b) and 6. When the *in situ* cell is charged beyond the second inflection point on the voltage curve (corresponding to  $\sim 1.38$  V or  $Na_{\sim 0.58}TiO_2$ ) into region III, the intensities of the superstructure peaks observed in the previous two regions gradually weaken. After the *in situ* cell is charged up to the third inflection point on the voltage curve (corresponding to 1.54 V or  $Na_{\sim 0.5}TiO_2$ ), all the superstructure peaks observed in regions I and II disappear from the *in situ* XRD spectra.

## Discussion

In contrast to a previous report we find a reversible capacity of  $152 \text{ mA h g}^{-1}$  for O3  $NaTiO_2$  which corresponds to the exchange of  $\approx 0.5$  Na in the voltage window 0.6–1.6 V. The increase in capacity from a previous report<sup>19</sup> is due to the widened low voltage window that is likely achieved by minimizing the water concentration in the recent electrolyte.

The rate capability of  $NaTiO_2$  is remarkably high, considering the micro-sized particles. This observation led us to re-investigate the previously reported diffusion barrier for Na in  $NaTiO_2$ . As Fig. 7 demonstrates, our DFT calculations find a Na migration barrier less than 224 meV in both O3 and O'3 phases,

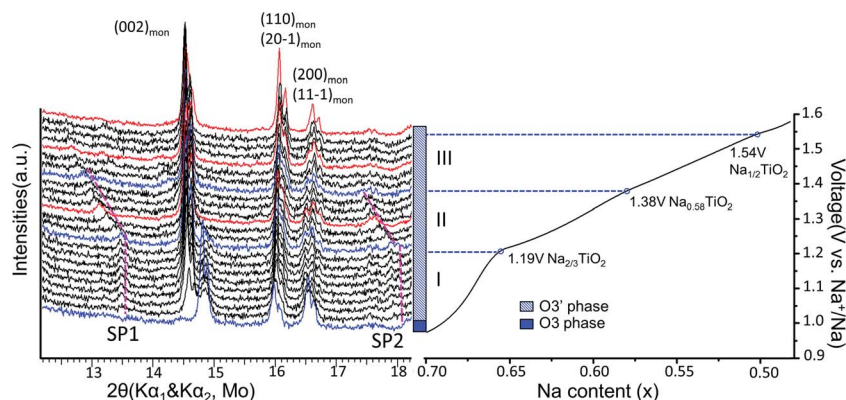


Fig. 6 Superstructure evolution from *in situ* XRD during electrochemical test. *In situ* XRD was collected during PITT charge of 0.03 V step size with 4 h (blue and black) or 10 h (red) scan per spectrum. The purple dashed lines represent the evolution of the superstructures (SP1 and SP2). The galvanostatic charge curve is shown on the right to illustrate the three regions divided by the inflection points explained in Fig. 5, as represented by the blue XRD spectra and dashed lines.

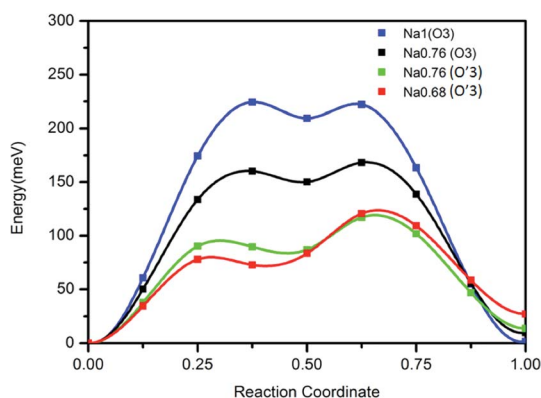


Fig. 7 Calculated diffusion barrier for Na in the O3 and O'3 phases using the di-vacancy mechanism. Details of the calculation are given in the Methods.

which is remarkably low, but consistent with the excellent rate capability observed experimentally. The calculated diffusion barrier of 750 meV reported earlier<sup>44</sup> may not have considered the di-vacancy diffusion mechanism which is known to be the operating mechanism for Na and Li migration in all O3 compounds.<sup>36,37</sup> The rate capability of NaTiO<sub>2</sub> is better than some other O3-type layered materials, such as NaMnO<sub>2</sub>, NaCoO<sub>2</sub> and NaNiO<sub>2</sub>, which all have stepwise voltage profiles.<sup>21–23</sup> It has been speculated that the two-phase boundary movement at these voltage plateaus slows down the Na insertion kinetics.<sup>28</sup> Our *in situ* XRD results of NaTiO<sub>2</sub> in Fig. 4 indicate that most regions are single phase, yielding a smooth voltage profile, while the two-phase reaction is limited to a short 0.94 V plateau, at which the O3 phase transforms into the O'3 phase through a monoclinic distortion.

The phenomenon of constant interslab distance in the O'3 single-phase region upon deintercalation is very unusual. Normally, the interslab distance changes continuously in the single-phase domain of layered compounds, but remains constant in the biphasic domain,<sup>14,15,24–26,38</sup> similar to the  $c_{\text{hex}}$  parameter variation of the O3 Na<sub>x</sub>TiO<sub>2</sub> phase discussed above.

Furthermore, this phenomenon can not be explained by the commensurate Na orderings or superstructures that are often observed,<sup>26,27</sup> as for a given commensurate superstructure the positions of superstructure peaks can not shift beyond the level of the lattice parameter variation. The large shift of superstructure peaks as shown in Fig. 5(b) and 6 is therefore likely to come from the change in modulation period of the ordering itself, as is sometimes observed in metallic alloys.<sup>39</sup> The fact that the peak shift in XRD is continuous points towards rather uncommon incommensurate Na orderings, as has been observed in a few other layered oxides.<sup>40,41</sup> If the modulation includes a composition component, the variation of modulation wavelength may be able to accommodate the complete Na composition range of the O'3 phase, without any significant change in slab spacing.

The correlation between the electrochemical voltage profile and the evolution of the ordering superstructure shown in Fig. 6 suggests that the O'3 region actually corresponds to three domains with different superstructure modulations. Domain I, the inception stage of the single O'3 phase, may correspond to the formation of Na<sub>2/3</sub>TiO<sub>2</sub> ordering. In domain II, the significant shift of the superstructure peaks may indicate an unusual incommensurate superstructure,<sup>40,41</sup> which shares an ordering pattern similar to Na<sub>2/3</sub>TiO<sub>2</sub> but with increasing modulation length and decreasing Na content down to Na<sub>0.58</sub>TiO<sub>2</sub>. Domain III might be a “biphasic domain” of two competing phases of the incommensurate Na<sub>2/3</sub>TiO<sub>2</sub>-like ordering with decreasing Na content from 0.58 further down to 0.5 and the possible formation of a solid solution phase. At 50% desodiation level, the superstructure phase likely transforms back into a solid solution phase. Moreover, no voltage plateau or step was observed around Na<sub>0.5</sub>TiO<sub>2</sub>, giving no evidence for the existence of a typical Na<sub>0.5</sub>TMO<sub>2</sub> ordering.<sup>29</sup> Therefore, the constant 1st derivative of the capacity over voltage in region III of Fig. 5(b) may suggest the competition between the superstructure phase observed by our *in situ* XRD and a solid solution phase upon Na de-intercalation, consistent with the observed transition from the monoclinic phase back to the rhombohedral phase.



It is worth noting that the actual percentage of lattice parameter variations in the layered O3 or P2 compounds is usually twice larger than the calculated volume expansion rate, with the shrinkage in the *ab* plane compensated in part by expansion in the *c* direction, corresponding to an obvious elongation of the crystal.<sup>15</sup> The special modulation of superstructures in the O'3 phase region of Na<sub>x</sub>TiO<sub>2</sub>, however, is coupled to the extremely small variation of the lattice parameters, as observed in Fig. 5, corresponding to a negligible volume expansion of approximately 0.4% (Fig. S5†). The excellent cyclability of NaTiO<sub>2</sub> might partially originate from its peculiar structural evolution. Similar large shifts of superstructure peaks coupled to very small lattice parameter variations in the single-phase domains were observed in certain composition ranges of Na<sub>x</sub>VO<sub>2</sub>,<sup>26</sup> which we believe may also be caused by an incommensurate superstructure evolution. Thus, the phenomenon is not limited to the Ti based system. Designing layered compounds that can show incommensurate superstructure or its competition with a solid solution phase in a large Na composition range might be a challenging but promising direction for both cathode and anode applications with improved structural stability upon Na intercalation.

## Conclusion

In summary, O3-NaTiO<sub>2</sub> was synthesized and tested electrochemically as an anode material for sodium-ion batteries. Approximately 0.5 Na can be reversibly intercalated in NaTiO<sub>2</sub>, corresponding to a reversible capacity of 152 mA h g<sup>-1</sup>. To achieve high capacity and the best cyclability, the optimal voltage window for galvanostatic cycling is 0.6–1.6 V. In addition, the sodium insertion/extraction mechanism was investigated using *in situ* X-ray diffraction. A reversible O3 to O'3 phase transition was observed. Special Na vacancy orderings were observed to be coupled with the unusual lattice parameter variation, which yields a constant interslab distance and slightly changing in-plane Ti–Ti distance in the O'3 phase. With its high capacity and excellent cyclability, NaTiO<sub>2</sub>, which consists only of earth-abundant elements, is a promising intercalation anode material for sodium-ion batteries.

## Methods

### Solid-state synthesis of NaTiO<sub>2</sub>

O3-type NaTiO<sub>2</sub> was synthesized *via* a solid-state reaction. TiO<sub>2</sub> anatase (Sigma Aldrich, 99.99%) and freshly cut Na (Sigma Aldrich, 99.95%) with 10% excess were placed in a Swagelok stainless steel tube, which was sealed in an argon-filled glove box. The tube was then fired at 920 °C for 12 hours in a flow of argon gas. After cooling, the tube was opened in the glove box to prevent exposure to air and moisture.

### Material characterization

The X-ray diffraction (XRD) patterns were collected on a Rigaku RU300 rotating anode diffractometer equipped with Cu Kα<sub>1</sub> radiation in the 2θ range of 10°–85°. All the samples were sealed

with Kapton film to avoid air exposure. Rietveld refinement and profile matching of the powder diffraction data of the as-prepared NaTiO<sub>2</sub> were performed using PANalytical X'Pert High Score Plus. The morphology of the as-prepared NaTiO<sub>2</sub> was examined using a Zeiss Merlin scanning electron microscope.

### Electrochemical tests

The active material of NaTiO<sub>2</sub>, the conductive agent carbon black (Timcal, Super P) and polyethylenetetrafluoride (PTFE) binder were manually mixed in a glove box with a weight ratio of 80 : 15 : 5 and then rolled into a thin film. The electrolyte was prepared by dissolving anhydrous NaPF<sub>6</sub> (98%, Sigma Aldrich) into ethylene carbonate:diethylcarbonate (EC:DEC) solution (anhydrous Sigma Aldrich, 1 : 1 in volume ratio). The as-prepared electrolyte exhibited a water level of approximately 5 ppm and was further dehydrated using 20 wt% molecular sieves with continuous rotation for two days. A Na metal film was used as the counter electrode. Swagelok cells were assembled in an argon-filled glove box with the oxygen and moisture levels being less than 0.1 ppm. The cells were tested on a Maccor 2200 or Arbin BT2000 operating at room temperature. The loading density of the active material was maintained at approximately 3 mg cm<sup>-2</sup>.

### *In situ* X-ray diffraction

*In situ* X-ray diffraction experiments during electrochemical testing of the batteries were performed on a Bruker D8 Advance Da Vinci Mo-source diffractometer scanned between 6.5°–30.5° 2θ range. An *in situ* battery was designed with a Be window for X-ray penetration. The battery was configured with a NaTiO<sub>2</sub> electrode as the working electrode, sodium as the counter electrode, 1 M NaPF<sub>6</sub>/EC:DEC as the electrolyte and glass fiber as the separator. The charge/discharge of the *in situ* battery was performed on a Solartron electrochemical potentiostat in the voltage range of 0.5–1.6 V at a current rate of C/20, or during potentiostatic intermittent titration technique (PITT) charge with a step size of 30 mV and step duration of 4 or 10 hours.

### DFT simulation

First principles calculations were performed in Generalized Gradient Approximations (GGA) to Density Functional Theory (DFT) using Vienna *ab initio* simulation package (VASP). Na diffusion barriers were calculated using the Nudged Elastic Band (NEB) method with the di-vacancy diffusion mechanism implemented in a 3 × 3 × 2 supercell corresponding to the composition of Na<sub>8/9</sub>TiO<sub>2</sub>. Na diffusion barriers in Na<sub>8/9</sub>TiO<sub>2</sub> were investigated with four different lattice parameters. Firstly, the lattice parameters of fully sodiated phase O3 Na<sub>1</sub>TiO<sub>2</sub> were fully relaxed by DFT and then fixed for NEB calculations. Three other lattice parameters are obtained by magnifying DFT relaxed O3 Na<sub>1</sub>TiO<sub>2</sub> lattice parameters proportional to the experimental ratios (obtained from *in situ* XRD) between O3 Na<sub>1</sub>TiO<sub>2</sub>, O3 Na<sub>0.76</sub>TiO<sub>2</sub>, O'3 Na<sub>0.76</sub>TiO<sub>2</sub> and O'3 Na<sub>0.68</sub>TiO<sub>2</sub>.

## Acknowledgements

This work was supported by the Samsung Advanced Institute of Technology.

## References

- 1 S.-W. Kim, D.-H. Seo, X. Ma, G. Ceder and K. Kang, *Adv. Energy Mater.*, 2012, **2**, 710.
- 2 H. Pan, Y.-S. Hu and L. Chen, *Energy Environ. Sci.*, 2013, **6**, 2338.
- 3 M. Dahbi, N. Yabuuchi, K. Kubota, K. Tokiwa and S. Komaba, *Phys. Chem. Chem. Phys.*, 2014, **16**, 15007.
- 4 S. P. Ong, V. L. Chevrier, G. Hautier, A. Jain, C. Moore, S. Kim, X. Ma and G. Ceder, *Energy Environ. Sci.*, 2011, **4**, 3680.
- 5 P. Ge and M. Foulletier, *Solid State Ionics*, 1988, **30**, 1172.
- 6 S. Komaba, W. Murata, T. Ishikawa, N. Yabuuchi, T. Ozeki, T. Nakayama, A. Ogata, K. Gotoh and K. Fujiwara, *Adv. Funct. Mater.*, 2011, **21**, 3859.
- 7 A. Darwiche, C. Marino, M. T. Sougrati, B. Fraisse, L. Stievano and L. Monconduit, *J. Am. Chem. Soc.*, 2012, **134**, 20805.
- 8 S. Komaba, Y. Matsuura, T. Ishikawa, N. Yabuuchi, W. Murata and S. Kuze, *Electrochem. Commun.*, 2012, **21**, 65.
- 9 L. Wu, X. Hu, J. Qian, F. Pei, F. Wu, R. Mao, X. Ai, H. Yang and Y. Cao, *Energy Environ. Sci.*, 2014, **7**, 323.
- 10 V. L. Chevrier and G. Ceder, *J. Electrochem. Soc.*, 2011, **158**, A1011.
- 11 Y. Xu, E. Memarzadeh Lotfabad, H. Wang, B. Farbod, Z. Xu, A. Kohandehghan and D. Mitlin, *Chem. Commun.*, 2013, **49**, 8973.
- 12 A. Rudola, K. Saravanan, C. W. Mason and P. Balaya, *J. Mater. Chem. A*, 2013, **1**, 2653.
- 13 P. Senguttuvan and M. R. Palacín, *Chem. Mater.*, 2011, **23**, 4109.
- 14 Y. Sun, L. Zhao, H. Pan, X. Lu, L. Gu, Y.-S. Hu, H. Li, M. Armand, Y. Ikuhara, L. Chen and X. Huang, *Nat. Commun.*, 2013, **4**, 1870.
- 15 Y. Wang, X. Yu, S. Xu, J. Bai, R. Xiao, Y.-S. Hu, H. Li, X.-Q. Yang, L. Chen and X. Huang, *Nat. Commun.*, 2013, **4**, 2365.
- 16 C. Fouassier, G. Matejka, J.-M. Reau and P. Hagenmuller, *J. Solid State Chem.*, 1973, **537**, 532.
- 17 C. Delmas, J.-J. Braconnier, C. Fouassier and P. Hagenmuller, *Solid State Ionics*, 1981, **4**, 165.
- 18 J.-J. Braconnier, C. Delmas and P. Hagenmuller, *Mater. Res. Bull.*, 1982, **17**, 993.
- 19 A. Mazzaz, C. Delmas and P. Hagenmuller, *J. Inclusion Phenom.*, 1983, **1**, 45.
- 20 A. Mendiboure, C. Delmas and P. Hagenmuller, *J. Solid State Chem.*, 1985, **331**, 323.
- 21 S. Komaba, C. Takei, T. Nakayama, A. Ogata and N. Yabuuchi, *Electrochem. Commun.*, 2010, **12**, 355.
- 22 X. Ma, H. Chen and G. Ceder, *J. Electrochem. Soc.*, 2011, **158**, A1307.
- 23 P. Vassilaras, X. Ma, X. Li and G. Ceder, *J. Electrochem. Soc.*, 2012, **160**, A207.
- 24 N. Yabuuchi, M. Kajiyama, J. Iwatate, H. Nishikawa, S. Hitomi, R. Okuyama, R. Usui, Y. Yamada and S. Komaba, *Nat. Mater.*, 2012, **11**, 512.
- 25 R. Berthelot, D. Carlier and C. Delmas, *Nat. Mater.*, 2011, **10**, 74.
- 26 M. Guignard, C. Didier, J. Darriet, P. Bordet, E. Elkaïm and C. Delmas, *Nat. Mater.*, 2013, **12**, 74.
- 27 X. Li, X. Ma, D. Su, L. Liu, R. Chisnell, S. P. Ong, H. Chen, A. Toumar, J. Idrobo, Y. Lei, J. Bai, F. Wang, J. W. Lynn, Y. S. Lee and G. Ceder, *Nat. Mater.*, 2014, **13**, 586.
- 28 H. Yoshida, N. Yabuuchi and S. Komaba, *Electrochem. Commun.*, 2013, **34**, 60.
- 29 C. Didier, M. Guignard, C. Denage, O. Szajwaj, S. Ito, I. Saadoun, J. Darriet and C. Delmas, *Electrochem. Solid-State Lett.*, 2011, **14**, A75.
- 30 C. Delmas, C. Fouassier and P. Hagenmuller, *Phys. Lett. B*, 1980, **99**, 81.
- 31 S. J. Clarke, A. J. Fowkes, A. Harrison, R. M. Ibberson and M. J. Rosseinsky, *Chem. Mater.*, 1998, **10**, 372.
- 32 Y. Lei, X. Li, L. Liu and G. Ceder, *Chem. Mater.*, 2014, **26**, 5288.
- 33 J. Akimoto and H. Takei, *J. Solid State Chem.*, 1990, **85**, 31–37.
- 34 X. Lai, J. E. Halpert and D. Wang, *Energy Environ. Sci.*, 2012, **5**, 5604.
- 35 M. Hillert, *Phase Equilibria, Phase Diagram and Phase Transformations*, Cambridge University Press, Cambridge, 1998.
- 36 A. Van Der Ven and G. Ceder, *Electrochem. Solid-State Lett.*, 2000, **3**, 301.
- 37 A. Van der Ven, J. Bhattacharya and A. A. Belak, *Acc. Chem. Res.*, 2013, **46**, 1216.
- 38 C. Didier, M. Guignard, J. Darriet and C. Delmas, *Inorg. Chem.*, 2012, **51**, 11007.
- 39 G. Ceder, D. de Fontaine, H. Dreyse, D. M. Nicholason, G. Stocks and B. L. Gyorffy, *Acta Metall. Mater.*, 1990, **38**, 2299.
- 40 H. Yang, Y. Shi, X. Liu, R. Xiao, H. Tian and J. Li, *Phys. Rev. B: Condens. Matter Mater. Phys.*, 2006, **73**, 014109.
- 41 M. D. Kirk, J. Nogami, A. A. Baski, D. B. Mitzi, A. Kapitulnik, T. H. Geballe and C. F. Quate, *Science*, 1988, **242**, 1673.